MPINet: Multiscale Physics-Informed Network for Bearing Fault Diagnosis With Small Samples

Chao Gao, Zikai Wang ⦿, *Graduate Student Member, IEEE*, Yongjin Guo ⦿, Hongdong Wang ⦿, and Hong Yi

Abstract—**Deep learning is increasingly prevalent in the bearing fault diagnosis, while the deficiency of fault samples could diminish the diagnostic efficacy of data-driven models that depend on extensive training data. For that, a novel multiscale physics-informed network (MPINet) is proposed for bearing fault diagnosis with small samples. Our fundamental idea is incorporating physical knowledge into the training process for enabling the model could better learn the fault features. To pursue this goal, a physics-informed block (PIB) is developed to extract fault features, which is customized for each failure mode. By this process, multiple independently trained PIBs encode the physical knowledge of their corresponding failure mode into the model, and thus yield multiscale fault features. Finally, the diagnosis result is obtained by using a new classifier head to merge these multiscale features. Extensive experimental results show that our MPINet can obtain superior diagnosis performance with small samples.**

Index Terms—**Bearing fault diagnosis, multiscale, physics-informed, small-sample learning.**

I. INTRODUCTION

BEARINGS are critical components of rotating machinery, which are prone to failure due to the material aging, high temperature, pulsating load, and so on [1]. Therefore, it is necessary to perform real-time condition monitoring and fault diagnosis of bearings to avoid high maintenance costs and potential hazards. Various methods have been proposed for fault diagnosis, including vibration signal analysis [2], [3], thermal imaging [4], [5], [6], acoustic signal analysis [7], [8], etc. Vibration analysis provides detailed fault information with high sensitivity, but it requires meticulously designed signal processing and can be affected by environmental noise. Acoustic analysis is a noninvasive and cost-effective method, yet it is

susceptible to noise. Thermal imaging offers the advantage of noncontact and real-time monitoring, while this kind of methods relies on expensive devices, and the measurement accuracy might be influenced by the distance between objects and monitoring devices. In this study, we focus on providing a novel deep-learning framework for fault diagnosis on small-sample vibration signals.

Nowadays, some deep learning methods have obtained fruitful achievements in the field of bearing fault diagnosis due to its strong feature extraction capabilities. Being a data-driven approach, deep learning models can achieve superior performance with sufficient training data. However, in practical scenarios, machine bearings are typically replaced promptly upon failure, leading to a scarcity of historical bearing fault samples. This lack of fault samples can potentially result in overfitting, thereby degrading the diagnostic performance of deep learning models. Consequently, three categorical strategies have been proposed to solve the small sample problem, including: 1) data augmentation; 2) transfer learning (TL) or metalearning (ML); and 3) model improvement. In what follows, these strategies are introduced and discussed in detail.

First, regarding the data augmentation strategy, its objective is to enhance the learning capability of diagnostic models for fault features by expanding the training dataset. Recently, advanced technologies and generation models, such as the synthetic minority oversampling technique [9], variational auto-encoder [10], and generative adversarial networks [11], have been applied to generate new data based on the limited realistic data. While additional generated data could introduce noise or unrealistic samples, and further lead to performance decreasing. Second, the strategy based on TL or ML utilizes diagnostic knowledge learned from other domains to help build learning models with stronger generalization performance. In [12], a feasible approach based on TL was proposed to perform the bearing diagnosis task with limited samples. The prior knowledge is learned from extensive data simulated by a dynamic model. The authors in [13] developed a task-sequencing ML method, achieving enhanced knowledge adaptation by gradually increasing the difficulty of the metatraining tasks. Despite the effective acceleration of the model's learning process for the target task using existing knowledge, its performance still depends on the quality of the source domain data and the choice of the model. Third, specific network structures or tricks are employed to optimize the feature extraction process of models and alleviate overfitting. Liang et al. [14] presented a multibranch and multiscale dynamic convolutional neural network (CNN), effectively improving the classification accuracy through its feature splitting strategy and channel reconstruction attention mechanism. Plakias and Boutalis [15] combined the dense convolutional blocks with an

attention mechanism, significantly reducing the parameters to be trained in the model and mitigating overfitting. These methods are capable of directly optimizing small sample problems without the need for additional data or knowledge, however they may not be suitable for tackling complex problems. In such scenarios, achieving ideal results may necessitate significant research and experimental costs.

Indeed, the aforementioned approaches have achieved some success in addressing small sample problems. However, they are all purely data-driven approaches; i.e., all fault-related features are learned from existing data without considering the actual information of the diagnosed bearing. Such that certain disturbances imposed on the bearing might result in physically inconsistent (or implausible) predictions [16], e.g., a false alarm could occur when the rocking of a ship underway has a slight effect on the bearing vibration signals. Maruthi and Hegde [17] mentioned that the characteristic frequency related to a specific bearing fault can be obtained from the peak position of the power spectrum of the collected vibration signals. Actually, this frequency can also be calculated based on the rotational speed and geometric shape of the target bearing, thereby serving as part of the physical knowledge about the bearing fault characteristics. This knowledge can be useful and even essential to assist purely data-driven models in extracting more characteristic frequency information with limited samples. Therefore, more attention should be paid to integrating valuable diagnostic information from the bearing physical knowledge into the model architecture.

To address this fundamental issue, we innovatively incorporate the physical knowledge into the bearing fault diagnosis with small samples and propose our multiscale physics-informed network (MPINet). The core of our proposed MPINet is a physics-informed block (PIB) which is tailored to each failure mode and is designed for feature extraction; i.e., each failure mode has one independently-designed PIB which is trained by using the specified physical knowledge associated with this failure mode. To be specific, for each failure mode in the targeted diagnostic task, a corresponding PIB needs to be designed. Based on the specific bearing fault characteristic frequency, a new physics kernel is generated to replace the data-driven kernel of the first convolutional layer of a conventional CNN, resulting in a PIB. The developed PIB needs to be trained with matched training dataset at each failure mode. After training, multiple PIBs are jointly used in the MPINet for processing the input signal to obtain multiscale fault features. The output features are then merged and further processed within the classifier head, which contains a multiscale feature fusion structure. The key contributions of our work are summarized as follows.

1) *A novel fault diagnosis methodology* that consists of a failure mode-dependent feature extraction block to obtain fault features specific to different failure modes, a training approach to train feature extraction blocks by generating a training dataset associated with each failure mode, and a network constructed with multiple trained feature extraction blocks.

2) *A feature extractor block* which is conducted by adding the physics-informed convolutional layer to the front part of a conventional CNN model, termed the PIB. This block incorporates the prior physical knowledge of specific bearing failure mode into the learning process, making the

model physically meaningful; i.e., improving the feature extraction capability of the model with small samples.

3) *A multiscale physics-informed network*, in which a novel structure that consists of multiple PIBs rather than a conventional single feature extractor is developed and used for effectively extracting multiscale fault features, namely, the MPINet. Furthermore, a classifier head with multiscale feature fusion structure is designed, which facilitates the information transfer between different PIBs and also enhances the learning capability of the model.

The rest of this article is organized as follows. In Section II, the detailed discussion of our proposed MPINet is presented. In Section III, two diagnostic cases of bearing datasets are conducted to validate the effectiveness of the proposed MPINet with small samples. Finally, Section IV concludes this article.

II. METHODOLOGY

A. Overview of the Fault Diagnosis Framework

To effectively reduce the complexity of multiclass classification problems, multiple feature extractors (i.e., the PIBs), instead of a conventional single extractor, are exploited to design the feature extraction stage of our proposed MPINet. Each PIB is dedicated to feature extraction for a specific failure mode (or fault type) in the diagnostic task. The extracted multiscale features are then fused and processed in a new classifier head to generate the final diagnostic results.

Suppose a bearing has k failure modes. In our diagnostic scheme, k corresponding $\{\mathrm{PIB}_i\}_{i=1}^{k}$ and 1 MPINet need to be generated. The PIB_i is exclusively designed for the ith failure mode of the task, aiming to reflect its specific fault characteristics. The final diagnostic model, MPINet, is composed of multiple trained $\{\mathrm{PIB}_i'\}_{i=1}^{k}$ and the classifier head $\mathcal{N}$, as shown in the red dashed box on the left side of Fig. 1. Following the basic idea of our proposed MPINet, the overall fault diagnosis framework is designed. It consists of three stages: 1) the offline training stage; 2) the online testing stage; and 3) the online diagnosis stage. The block diagrams of these three stages are jointly depicted in Fig. 1 and described in what follows.

For the offline network training stage (i.e., Stage 1 in Fig. 1), two steps are sequentially performed, including: 1) training datasets construction. In this step, the collected raw bearing fault data samples are used to construct different training datasets, namely, Dataset j ($j = 1, 2, \ldots, k + 1$), corresponding to PIB_i and MPINet. Datasets 1 to k are constructed with two labels for PIBs and Dataset $k + 1$ is constructed with k labels for MPINet; 2) model training. Each feature extractor (i.e., $\mathrm{PIB}_1, \mathrm{PIB}_2, \ldots, \mathrm{PIB}_k$) is subject to be trained independently using the matched dataset in Datasets 1 to k. Then, the MPINet is trained using Dataset $k + 1$ with the PIB layer frozen.

In the online testing stage (i.e., Stage 2 in Fig. 1), the performance of the trained MPINet' is verified with labeled monitoring data.

As for the online diagnosis stage (i.e., Stage 3 in Fig. 1), TL technology is utilized. The pretraining parameters are loaded to initialize the weights and biases of the model. Then, the classifier head $\mathcal{N}$ of the MPINet is fine-tuned by using a small amount of real data. This process yields a diagnosis model for real scenarios, thereby enabling timely fault detection and identification.
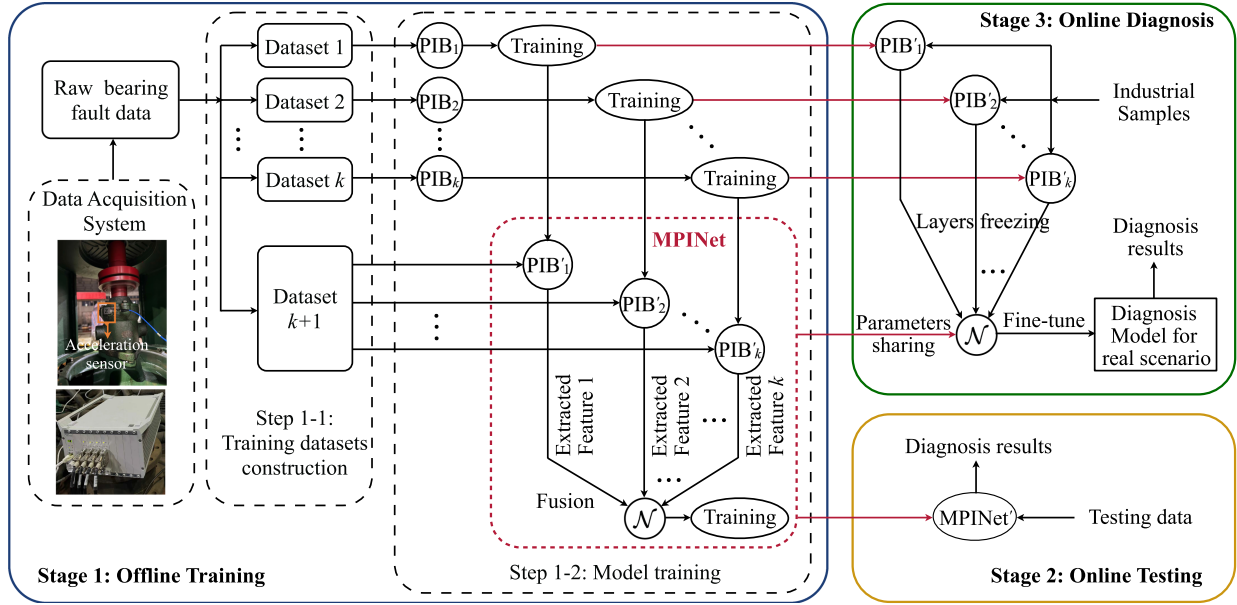
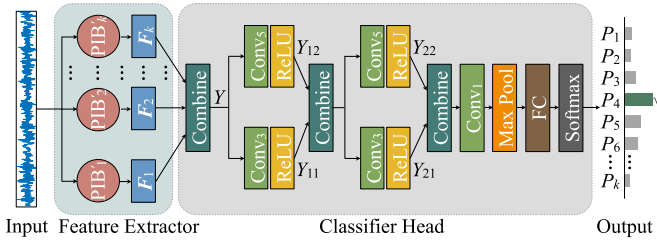Fig. 1. Fault diagnosis framework of the proposed MPINet.

Fig. 2. Architecture of the proposed MPINet.

In the following section, we shall describe our designed fault diagnosis model (i.e., the MPINet) and feature extractor (i.e., the PIB_i), as well as the training approach for each PIB_i and the MPINet.

B. Multiscale Physics-Informed Network (MPINet)

As depicted in Fig. 2, our developed MPINet has two parts: 1) feature extractor based on multiple PIBs; and 2) classifier head based on a CNN with multiscale feature fusion structure. They are described in detail as follows.

1) Feature Extractor: Feature extraction is performed using multiple trained PIBs, thereby obtaining multiscale features associated with each fault type in the target diagnostic task. As illustrated in Fig. 2, the raw vibration signals of a bearing are simultaneously fed into the trained $\{\text{PIB}'_i\}_{i=1}^{k}$. Then, multiscale fault features are obtained and labeled as $\boldsymbol{F}_1, \boldsymbol{F}_2, \ldots,$ and $\boldsymbol{F}_k$.

2) Classifier Head: Following the feature extractor, a classifier head is constructed and utilized to process the extracted features, resulting in the final diagnostic results. The output multiscale features of PIBs are first fused in a feature fusion layer to facilitate information exchange among them. Subsequently, the fused features are further enhanced by exploiting several dual path convolution modules, inspired by the inception architecture [18]. The utilization of convolutional layers with kernel

sizes of 3 and 5 enables the extraction of fault features across both fine and coarse receptive fields. More details of the classifier head are described as follows.

As shown in Fig. 2, the output features of multiple PIBs, i.e., $\boldsymbol{F}_1, \boldsymbol{F}_2, \ldots,$ and $\boldsymbol{F}_k$, are first concatenated in the "Combine" layer. Thus, a new representation $\boldsymbol{Y}$, i.e., $[\boldsymbol{F}_1, \boldsymbol{F}_2, \ldots, \boldsymbol{F}_k]_F$, is produced. The symbol $[\cdot, \cdot]_F$ denotes a feature-wise concatenation operation; i.e., the concatenation is fulfilled along the feature dimension. As a result, if each $\boldsymbol{F}_i$ $(i = 1, 2, \ldots, k)$ has a dimension of (C_1, H_1), then the dimension of $\boldsymbol{Y}$ will be (C_1, kH_1), where C_1 represents the number of feature channels and H_1 denotes the length of the 1-D feature. The feature set $\boldsymbol{Y}$ is then fed into two convolutional layers with different kernel sizes simultaneously, obtaining

$$\boldsymbol{Y}_{11} = \text{ReLU}\left(\text{Conv}_3(\boldsymbol{Y})\right), \tag{1}$$

$$\boldsymbol{Y}_{12} = \text{ReLU}\left(\text{Conv}_5(\boldsymbol{Y})\right) \tag{2}$$

where $\text{Conv}_n(\cdot)$ denotes a convolutional layer with the kernel size of n; $\text{ReLU}(x) = \max(x, 0)$ represents the ReLU activation function. Assuming that there are C_2 kernels in the two layers, the dimensions of $\boldsymbol{Y}_{11}$ and $\boldsymbol{Y}_{12}$ will be (C_2, kH_1). The obtained $\boldsymbol{Y}_{11}$ and $\boldsymbol{Y}_{12}$ are then combined for fusing the features across the fine and coarse receptive fields, resulting in a new representation $[\boldsymbol{Y}_{11}, \boldsymbol{Y}_{12}]_C$ with a feature map of $(2C_2, kH_1)$. The symbol $[\cdot, \cdot]_C$ represents a channel-wise concatenation operation. Subsequently, $[\boldsymbol{Y}_{11}, \boldsymbol{Y}_{12}]_C$ is fed into another pair of convolutional layers; i.e.,

$$\boldsymbol{Y}_{21} = \text{ReLU}\left(\text{Conv}_3([\boldsymbol{Y}_{11}, \boldsymbol{Y}_{12}]_C)\right), \tag{3}$$

$$\boldsymbol{Y}_{22} = \text{ReLU}\left(\text{Conv}_5([\boldsymbol{Y}_{11}, \boldsymbol{Y}_{12}]_C)\right). \tag{4}$$

The yielded new feature $[\boldsymbol{Y}_{21}, \boldsymbol{Y}_{22}]_C$ is further processed using a Conv_1 layer to merge the characteristics from various channels within it. Finally, the feature will be sequentially fed into a max pooling layer, a fully connected (FC) layer and a Softmax layer to produce a k-dimensional output feature $\boldsymbol{P}$. Each element in the feature set $\boldsymbol{P} = \{P_1, P_2, \ldots, P_k\}$ represents the probability
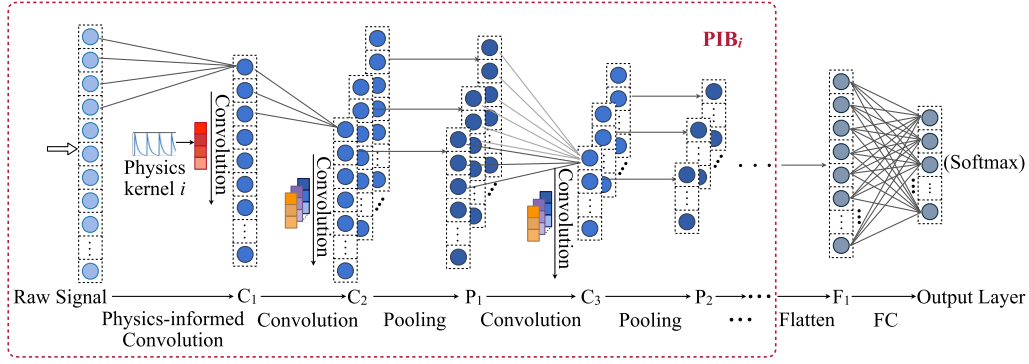
Fig. 3. Structure of a binary network nested with PIB_i.

C. Physics-Informed Block (PIB)

According to Section II-A, the trained PIB $'_i$ is supposed to extract the typical characteristics of the ith fault type in a k-class diagnostic task. This can be conducted by nesting the block into a network with a binary classifier, and training the network to distinguish the ith fault type from the others.

1) The Outline of PIB: The structure of the binary network nested with a PIB_i is depicted as Fig. 3, where the red dashed box is the PIB_i and the rest is the FC layer and the Softmax layer. As shown in Fig. 3, the proposed PIB_i architecture consists of multiple layers, among which the first layer is prebuilt based on the physical knowledge of bearing faults and the others are purely data-driven. The first layer, called the physics-informed convolutional layer, is the most special layer of the PIB_i. It incorporates the physical information of the ith failure mode into the feature extraction process by quantifying the similarity between the input signals and the fault characteristic signals. The ith physics kernel in this layer is pregenerated based on the specific fault characteristic frequency of the ith failure mode. Therefore, no additional hyperparameters will be introduced in building the physics-informed layer. This feature makes it possible to improve the feature extraction capability of the network without increasing the training effort and the risk of overfitting.

For our targeted fault diagnosis task, it is necessary for the architecture and hyperparameters of each PIB_i to remain consistent to ensure that their output feature vectors are dimensionally compatible for the subsequent feature fusion in the MPINet. However, adjustments are required for the PIB_i in terms of its physics kernel, loss function, and training dataset depending on the ith failure mode, which will be elaborated further. Note that a physics kernel is not necessary for the PIB_i designed for a normal condition, as the clear distinction between normal and faulty states of the bearing.

2) The Establishment of PIB: The first physics-informed convolutional layer is the key part of our designed PIB. According to the convolution theorem, time-domain convolution of two signals is equivalent to their product in the frequency domain. Therefore, in our task of bearing fault diagnosis, the convolution operation essentially utilizes a kernel to extract the most critical frequency information in the input vibration signal; i.e., identifying the modulating frequency that are close to the fault characteristic frequency of the target bearing [19]. As such, the kernel can be predefined by an ideal simulated fault characteristic signal, which maps the physical fault characteristics of a bearing into the PIB. The reference signal generation mechanism is described below.

According to the bearing fault physics, if there is a localized single point defect in one surface of a bearing, a series of impulses will be generated as the rolling elements periodically pass over the defect. Therefore, given the fault characteristic frequency of a bearing, its fault vibration signals can be simulated by using the signal generation model [20] as

$$v(t) = a_0 q_0 d_0 \sum_{k=0}^{\infty} \left[\delta(t - k/f_d)\exp(-\xi(t - k/f_d)) \right] \quad (5)$$

where t is the time index; a_0 is the instant transfer function between the point at which the impulse was applied and the measurement location; q_0 is a constant load applied to the bearing; d_0 is a constant amplitude under a unit load, accounting for the fault severity; $\delta(\cdot)$ is the unit impulse function; ξ is the damping coefficient; and f_d is the fault characteristic frequency, which varies in terms of the bearing fault type, i.e., inner race fault (IF), outer race fault (OF), rolling element fault (RF), and fundamental cage fault (CF). By [21], f_d can be easily calculated by the rotating speed and geometry of target bearing as

$$f_d = \begin{cases} \frac{n}{2}\left(1 - \frac{d}{D_p}\cos\theta\right)f_r, & \text{for OF;} \\[2mm] \frac{n}{2}\left(1 + \frac{d}{D_p}\cos\theta\right)f_r, & \text{for IF;} \\[2mm] \frac{D_p}{2d}\left(1 - \left(\frac{d}{D_p}\cos\theta\right)^2\right)f_r, & \text{for RF;} \\[2mm] \frac{1}{2}\left(1 - \frac{d}{D_p}\cos\theta\right)f_r, & \text{for CF} \end{cases} \quad (6)$$

where n is the number of rolling balls, d denotes the diameter of the rolling element, D_p is the groove section size, θ is the contact angle, and f_r denotes the rotating frequency of the bearing, defined as $f_r = r/60$ with r is the rotation speed. Thus, (5) can be used to generate the physics kernel for different PIB_i. Fig. 4 illustrates the simulated physics kernels for various fault types. The output features of the physics-informed layer can be then obtained by convolving the input signal $x(t)$ with the generated kernel $v(t)$ as follows:

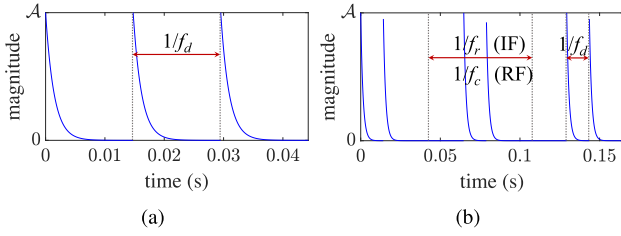$$x(t) \otimes v(t) = \sum_{k=0}^{K_w} x(t - k) \cdot v(k) \quad (7)$$

Fig. 4. Two Illustrative examples of physics kernels with characteristic frequency of f_d and rotating frequency of f_r ($A = a_0 q_0 d_0$). (a) Kernel for OF. (b) Kernel for IF or RF. Note that f_c denotes the fault frequency of CF in (6).

TABLE I
PARAMETERS OF THE CWRU AND MFPT EXPERIMENTAL BEARINGS, WHERE f_{r1} AND f_{r2} ARE THE ROTATING FREQUENCIES OF THE CWRU SHAFT AND MFPT SHAFT, RESPECTIVELY

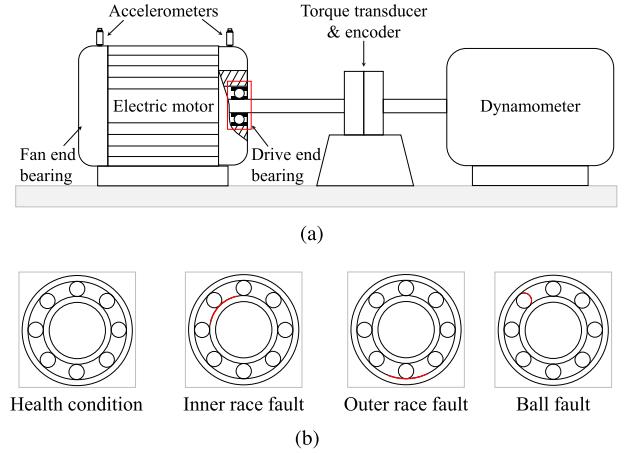| Parameters	CWRU bearing	MFPT bearing
Contact angle (°)	–	0
Number of balls	9	8
Roller diameter (mm)	7.94	5.97
Pitch Diameter (mm)	39.04	31.62
Ball pass frequency of inner race	$5.415 f_{r1}$	$4.755 f_{r2}$
Ball pass frequency of outer race	$3.585 f_{r1}$	$3.245 f_{r2}$
Ball (roller) spin frequency	$2.357 f_{r1}$	–

Fig. 5. Illustrative examples of (a) the test rig for CWRU and (b) the included drive end bearing components, i.e., the red rectangle in (a), with different fault locations which are highlighted in red.

where $\otimes$ is the convolution operator, t is the time index, and K_w is the width of the physics kernel.

During the definition of the kernel, it is essential for the kernel width to be much smaller than the length of the input signal to avoid the loss of valuable information within the signal. In addition, it is important to note that determining the precise values of a_0, q_0, and d_0 in (5) is challenging and time consuming in practice. As mentioned before, the physics kernel works by extracting the frequency information associated with the faulty bearing through convolution, with f_d in (5) playing a major role. The parameters a_0, q_0, and d_0 influence the kernel by altering its amplitude. Consequently, in (7), their effect on the convolution result of the input signal manifests as a linear scaling. This scaling impacts the gradient update of the PIB. However, the batch normalization operation we employ mitigates this effect. Therefore, for all used kernels, we set $a_0 = q_0 = d_0 = 1$.

D. Training Process

The training of the proposed MPINet involves two steps: 1) constructing the training datasets; and 2) sequentially training the feature extractors (i.e., the PIBs, in our case) and the diagnosis model (i.e., the MPINet).

Following our basic idea, i.e., the different contributions of PIBs and MPINet, it is necessary to construct matched training datasets for them during the offline training stage, respectively. Assuming that there are k fault types with n samples for each type, and thus we should establish $k + 1$ datasets—k datasets for the PIBs and 1 dataset for the MPINet, which are described in detail as follows. First, for the datasets used to train the PIBs, we construct a new partition for each used PIB. For example, for the ith fault type, its corresponding n samples are set to the positive examples (i.e., labeled with 1), and the $(k − 1)n$ samples with respect to other fault types are all set to the negative examples (i.e., labeled with 0). By repeating the aforementioned process for each fault type, the datasets for training our PIBs can be finally obtained. Second, since the MPINet is developed to conduct multiclass classification of fault types, the dataset for training our MPINet is constructed by annotating k fault types (each with n samples) with k distinct labels.

The optimization problem for the PIBs and MPINet involves minimizing their respective loss functions. The cross-entropy function is adopted as the loss function for both the PIBs and MPINet. To address the class imbalance problem during PIB training, the weight of positive samples is increased. Specifically, the ratio of the positive and negative samples, denoted as ω, is assigned to the term of positive samples in the loss function

of each PIB, formulated as

$$\text{Loss} = -\frac{1}{N} \sum_{i=1}^{N} \omega y_i \log p_i + (1 - y_i) \log(1 - p_i) \quad (8)$$

where N is the total number of samples, y_i is the true label of the ith sample, and p_i is the probability of the ith sample being predicted as a positive class by the PIB.

III. EXPERIMENTAL RESULTS

In this section, the proposed MPINet is validated on the Case Western Reserve University (CWRU) dataset [22] and the Machinery Failure Prevention Technology (MFPT) society dataset [23] for rolling bearing diagnosis. Table I documents the detailed bearing parameters of our used datasets.

A. Experimental Setups

1) Datasets Description: As shown in Fig. 5, the CWRU dataset [22] was collected from a motor-driven mechanical system, where Fig. 5(a) demonstrates the experimental rig and Fig. 5(b) shows the test bearings with different fault locations. To simulate different levels of fault severity, single-point defects with variant diameters were introduced on the drive end and fan end bearings of the motor. Each bearing is tested under four motor loads of 0, 1, 2, and 3 hp. The rotating speeds r that align
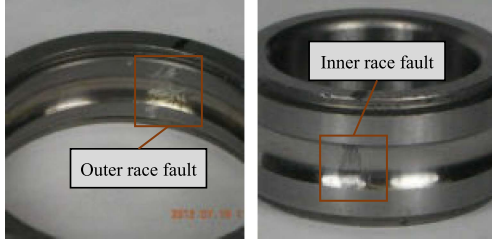
Fig. 6. Used fault bearing for MFPT test rig.

with these four motor loads, used in (6), are 1797, 1772, 1750, and 1730 r/min, respectively.

In this study, vibration signals from the drive end bearing, sampled at a frequency of 12kHz under four different loads, are used for model validation. These signals are used to construct four datasets, labeled CWRU0, CWRU1, CWRU2, and CWRU3, corresponding to motor loads of 0, 1, 2, and 3 hp, respectively. Each dataset includes ten kinds of bearing fault types for fault classification, labeled as follows:

1) Normal condition (NC), i.e., with no fault;
2) Ball fault with diameter of 0.007, 0.014, and 0.021 in (BF1, BF2, BF3);
3) IF with diameter of 0.007, 0.014, and 0.021 in (IF1, IF2, IF3);
4) OF with diameter of 0.007, 0.014, and 0.021 in (OF1, OF2, OF3).

The MFPT dataset [23], sourced from a bearing test rig, includes both normal bearing data and fault data under various load conditions. All data were collected at a speed of 1500 r/min. The experimental fault bearing is depicted in Fig. 6. For this study, normal bearing data sampled at 97656 Hz and fault data sampled at 48828 Hz were selected to create the dataset, referred to as MFPT. To ensure effective model training, all signals were resampled to 12 kHz. The classification utilizes five different fault types, including

1) NC at 270 lbs of load, termed N;
2) IF at 200 and 300 lbs of load, termed IF-1 and IF-2;
3) OF at 200 and 300 lbs of load, termed OF-1 and OF-2.

For training the proposed MPINet, each of the five datasets is reconstructed into $k + 1$ subdatasets, where k is set to 10 for datasets CWRU0–CWRU3 and 5 for dataset MFPT. In the $k + 1$ subdatasets, k subdatasets with 2 labels are provided for the corresponding PIBs, whereas 1 dataset with k labels is for the MPINet. For each subdataset, N and $9N$ samples are randomly taken from this subdataset as the training and the test set, respectively. A fixed number N/k of samples is assigned to each fault type. Each sample contains 1000 data points. To evaluate the diagnosis performance with small samples, N is set to 40, 60, 80, 100, and 120.

2) Implementation Details: To perform fault diagnosis on datasets CWRU0–CWRU3, 10 PIBs and 1 MPINet are created for each dataset. For dataset MFPT, 5 PIBs and 1 MPINet are generated. Before training, the physics kernel of each PIB is generated using (5). The parameters from Table I are utilized for calculating the bearing fault characteristic frequency f_d, and the reciprocal of the sampling frequency is employed as the time interval t. The first 2000 elements of the simulated signal serve as the physics kernel in the first layer (i.e., physics-informed

convolutional layer) of the PIB. In the offline training and online diagnosis stages, all samples in each dataset are used for training and test.

The detailed configuration of each PIB is introduced as follows. The input signals are padded with zeros for conducting the physics-informed convolution operation, resulting in a new representation of the same length. Then, four data-driven convolutional layers are employed, with kernel sizes of 24, 9, 3, and 3, and kernel numbers of 8, 16, 32, and 64. In these layers, no padding is used for each operation. The ReLU activation function and batch normalization of features is performed after each convolutional operation. The training of each PIB contains 30 epochs, and each epoch is based on a training batch that consists of 8 samples randomly selected from the used dataset. The Adam optimizer is used to solve the optimization problem, and the learning rate of this optimizer is set to 0.001. In the loss function, weight factors of 9 and 4 are assigned for training with the CWRU and MFPT datasets, respectively.

In our MPINet, the input signals are first processed by the trained PIBs, resulting in k sets of features. These features are then fed into the classifier head, in which two dual path convolution modules with kernel numbers of 128 and 512 are developed. The stride of each convolution operation is set to 1 for keeping the output size fixed. The training epoch and optimizer of the MPINet are identical to those of the PIB.

3) Comparison Methods: To evaluate the diagnostic performance of our MPINet under small samples, SVM [24], MLP [25], ResNet V2 [26], TICNN [27], and DANN [28] are implemented for comparisons. Except the DANN [28], codes of these methods provided by their respective authors are implemented with default parameters. For the DANN, its diagnostic accuracy results on the CWRU dataset reported in [28] are exploited.

B. Ablation Study

1) Phase-1 Study: To investigate the contribution of our developed multiscale fault feature extractor (PIBs) and classifier head, an ablation study is conducted on the datasets CWRU0–CWRU3. In this study, M_1 serves as the baseline, in which both the feature extractor and classifier from the proposed MPINet are replaced by multiple CNNs without the physics-informed convolutional layer and a probability comparison method,[1] respectively. Then, M_2 adds our multiple PIBs and M_3 adds our classifier head. In M_4, we replace the multiple CNNs of M_3 with a single PIB. M_5 is our proposed MPINet. The obtained diagnostic accuracies of these models under different training samples averaged on all the used datasets are presented in Table II.

One can see that, with integrating PIB, M_2 and M_5 outperform M_1 and M_3 by a large margin, respectively. This reveals the superior performance of the physics kernel in feature extraction under small sample conditions. Similarly, M_3 outperforms M_1, and M_5 outperforms M_2, indicating that the classifier head effectively utilizes the multiscale fault features from the feature extractor, thus improving diagnostic accuracy. Notably, M_3 achieves satisfactory diagnostic accuracy with a training sample size of 80–120. This suggests that the proposed design of

---

[1]The diagnostic result is obtained by selecting the output with the highest probability value among all the trained feature extractors using the probability comparison method.

TABLE II
DIAGNOSTIC ACCURACY (%) OF DIFFERENT MODELS UNDER DIFFERENT
TRAINING SAMPLES AVERAGED ON ALL THE USED DATASETS

	Feature extractor	Classifier head	Number of training samples				
			40	60	80	100	120
M_1	CNNs	–	28.24	38.93	45.46	51.61	53.77
M_2	PIBs	–	41.53	46.56	51.60	57.40	62.66
M_3	CNNs	✓	64.58	76.94	93.33	92.59	93.68
M_4	PIB	✓	70.00	80.14	86.98	92.50	95.21
M_5	PIBs	✓	**92.22**	**95.97**	**96.88**	**97.92**	**98.49**

TABLE III
COMPARISON RESULTS FOR DIFFERENT KERNEL AMPLITUDES AVERAGED
ON FOUR CWRU DATASETS

Amplitude of kernels	Number of training samples				
	40	60	80	100	120
1	92.22	95.97	96.88	97.92	98.49
1, 2, 3	91.39	96.53	95.98	97.15	98.97
Error	0.83	0.56	0.90	0.77	0.48

TABLE IV
COMPARISON OF DIFFERENT METHODS IN THE ACCURACY ON TRAINING
SET (FIRST ENTRY) AND TEST SET (SECOND ENTRY), AS WELL AS THE
ERROR BETWEEN THESE TWO SETS (THIRD ENTRY)

Methods	Number of training samples				
	40	60	80	100	120
SVM	100	100	100	100	100
	36.53	41.11	42.59	44.67	45.83
	63.47	58.89	57.41	55.33	54.17
MLP	82.50	100	100	100	100
	22.78	37.04	37.64	40.56	42.87
	59.72	62.96	62.36	59.44	57.13
ResNet V2	80.00	83.33	86.25	92.00	94.17
	68.61	80.74	82.08	88.89	92.04
	11.39	2.59	4.17	3.11	2.13
TICNN	35.00	58.33	76.25	86.00	98.33
	22.50	47.96	69.86	77.67	94.35
	12.50	10.37	6.39	8.33	3.98
MPINet	100	100	100	100	100
	96.94	98.33	99.17	99.78	99.72
	3.06	**1.67**	**0.83**	**0.22**	**0.28**

multiple feature extractors for specific faults enables the model to effectively extract multiscale fault features, even without a physical kernel. The same conclusion can be obtained by comparing M_4 and M_5.

2) Phase-2 Study: As we have mentioned in Section II, the amplitudes of used physics kernels are simplified to 1. Is this an appropriate approach for our diagnosis task? To answer this question, an experiment is conducted on the CWRU0–CWRU3 datasets. We first set all the kernel amplitudes to 1. Then, corresponding to different fault severities, the kernel amplitudes are set to 1, 2, and 3, respectively. The comparison of diagnosis accuracies averaged on four CWRU datasets are listed in Table III. From this Table, we can find that the amplitude of physics kernels has minimal impact on the final diagnosis results. This may be attributed to the fact that a corresponding PIB has been designed for each fault type, significantly reducing the impact of the physics kernel amplitude on feature extraction. However, if a strict match between kernel amplitude and fault severity is required, the processing becomes more complex as the number of fault types increases. To achieve sufficiently high diagnosis accuracy with a relatively simple kernel processing, the magnitude of each physics kernel is set to 1 for all of them.

C. Objective Evaluation

1) Performance on Small Samples: For a more intuitive understanding of the small sample challenge addressed in this study, we first compare the accuracies on the training set and test set of comparison methods with our MPINet. Table IV documents the results of all methods on dataset CWRU2. One can see that the classical methods, SVM and MLP, basically achieve accuracy of 100% on the training set, whereas only obtain about 40% average accuracy on the test set; i.e., suffering from the overfitting problem. As for the ResNet V2 and TICNN, thanks to their effective deep structures, they alleviate the overfitting phenomenon to some extent, while their performance still suffers from the limited training samples. In comparison to all the aforementioned models, our MPINet exhibits the smallest error in accuracy between the training set and test set at various small sample levels. The problems of overfitting and inadequate

diagnostic performance resulting from a lack of training samples can be successfully alleviated.

Fig. 7 presents the comparison results on all the five datasets. One can see that our proposed MPINet obtains the highest accuracy in all cases, demonstrating its superior diagnostic performance with small samples. This success is attributed to the physics-informed feature extractor and multiscale feature fusion, enabling MPINet to extract more valuable information from limited data. In contrast, SVM and MLP exhibit poor diagnostic performance due to their inadequate processing of raw signals, leading to insufficient feature extraction for complex pattern recognition tasks. TICNN and ResNet V2, benefiting from convolutional operations and model improvements (first-layer kernel dropout and enhanced residual connection, respectively), achieve comparable accuracy. However, their performance remains limited by the training data size. The adversarial training technique of DANN enhances the diagnostic performance with small samples. In addition, an interesting observation can be made when examining the accuracy differences at different training sample sizes for the same model. For example, with dataset CWRU0, our proposed MPINet shows a ratio of $0.90/0.9611 = 0.936$ when the number of training samples is 40 and 120. In comparison, the ratios for SVM, MLP, ResNet V2, TICNN, and DANN are 0.556, 0.643, 0.757, 0.308, and 0.898, respectively. Obviously, as training samples are reduced, MPINet exhibits greater robustness compared to other models, indicating a more stable diagnostic performance. This robustness is consistently observed in other cases as well. It indicates that the performance advantage of our proposed MPINet over other comparison methods becomes more pronounced when stricter requirements are imposed on the number of training samples.

2) Performance on Domain Adaptation: In this part, we evaluate the diagnostic performance of our proposed MPINet on domain adaptation (DA). Two kinds of DA tasks are conducted: 1) DA between different load conditions within the same bearing system by the CWRU0–CWRU3 datasets; and 2) DA between different bearing systems by the CWRU and MFPT datasets. For the first DA task, each dataset in CWRU0–CWRU3 is set up as a
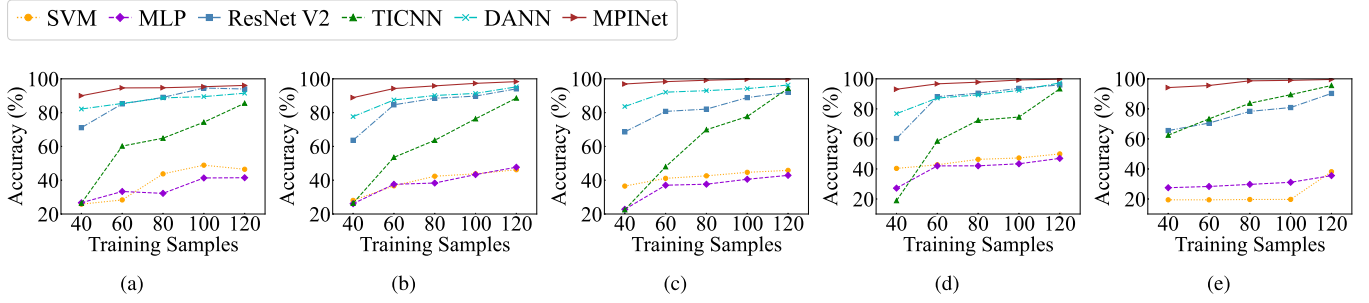
Fig. 7. Comparison results in five datasets, including (a) CWRU0, (b) CWRU1, (c) CWRU2, (d) CWRU3, and (e) MFPT.

TABLE V
DIAGNOSTIC ACCURACY (%) OF MPINET ON THE DA TASK AMONG THE CWRU DATASETS

Source → Target	Sample amount for fine-tuning				
	40	60	80	100	120
CWRU0 → CWRU1	95.00	95.56	95.69	96.11	96.67
CWRU0 → CWRU2	95.83	98.33	98.75	98.33	98.33
CWRU0 → CWRU3	92.50	97.78	98.33	98.67	99.17
CWRU1 → CWRU0	93.33	97.22	97.50	98.00	98.33
CWRU1 → CWRU2	94.17	98.33	98.61	98.00	99.35
CWRU1 → CWRU3	91.67	96.67	98.43	98.75	99.00
CWRU2 → CWRU0	95.00	97.04	97.36	97.00	98.06
CWRU2 → CWRU1	96.11	97.67	98.47	97.89	98.33
CWRU2 → CWRU3	99.17	99.44	99.58	99.22	99.58
CWRU3 → CWRU0	93.33	93.89	94.58	97.33	97.78
CWRU3 → CWRU1	96.94	97.22	98.33	99.00	99.06
CWRU3 → CWRU2	99.17	99.44	99.58	99.72	99.89

TABLE VI
DIAGNOSTIC ACCURACY (%) OF MPINET ON THE DA TASK BETWEEN THE CWRU AND MFPT DATASETS

Source → Target	Sample amount for fine-tuning				
	20	30	40	50	60
CWRU0† → MFPT*	93.44	95.79	98.36	99.36	98.91
CWRU1† → MFPT*	95.08	95.79	99.18	100	100
CWRU2† → MFPT*	91.80	94.74	99.18	100	100
CWRU3† → MFPT*	95.08	94.74	100	100	100
Average	93.85	95.27	99.18	99.84	99.73
MFPT* → CWRU0†	92.06	95.79	98.41	99.36	100
MFPT* → CWRU1†	98.41	98.95	99.21	100	99.46
MFPT* → CWRU2†	96.83	98.95	97.62	99.37	100
MFPT* → CWRU3†	98.41	93.68	97.62	100	100
Average	96.43	96.84	98.22	99.68	99.87

single domain, which results in 12 diagnostic scenarios. Refer to the second DA task, the data in CWRU0–CWRU3 and MFPT are reconstructed as three fault types (i.e., N, IF, and OF). Then, the reconstructed datastes are denoted as CWRU0†–CWRU3† and MFPT*. The specific fault types of our reconstructed CWRU datasets are relabeled as follows:

1) NC (NC†);
2) IF with diameter of 0.007–0.021 in (IF†);
3) OF with diameter of 0.007–0.021 in (OF†).

As for the MFPT* dataset, specific fault types contains the following:

1) N (N*);
2) IF at 200 and 300 lbs of load (IF*);
3) OF at 200 and 300 lbs of load (OF*).

Eventually, we obtain eight scenarios of fault diagnosis in the DA task between different bearing systems.

In the offline training stage, 120 samples from the source domain are used to generate the pretraining parameters. Subsequently, a small amount of samples from the target domain are utilized to fine-tune the whole model online. The diagnostic accuracies of two DA tasks are documented in Tables V and VI, respectively. It can be found that, even with a limited number of target domain samples, our proposed method has great performance on both DA tasks, achieving high accuracy averaged over 0.95. The accuracy almost keeps a consistent improvement as the number of target domain samples increased. In what follows, we analyze the experimental results in detail.

For the first DA task, the accuracy of the diagnosis improves as the load discrepancy between the target and source domains decreases. When diagnostic scenarios are with significant load changes, our MPINet maintains great diagnostic performance. For instance, one can see from Table V that the average difference between CWRU3→CWRU0 and CWRU3→CWRU1 is only 4.2%. For the second DA task, the proposed method effectively realizes diagnostic migration between different bearings. Additionally, the migration from MFPT to CWRU is less challenging than the reverse. As shown in Table VI, the former has improved accuracy by 0.63 (on average) compared to the latter. Note that the pre-training parameters of the feature extractor in MPINet are directly shared during the online diagnosis stage, with only the classifier head being fine-tuned. This indicates that our innovative configuration of multiple PIBs enables the extraction of multiscale fault features, despite discrepancy between the physical kernels of each PIB and the target domain. As a result, the feature extractor of MPINet exhibits highly robust and reliable performance.

D. Subjective Evaluation

In order to further reveal how the proposed MPINet functions, the t-distributed stochastic neighbor embedding technique is employed to project its output features of each layer into a two-dimensional space. The feature visualization results on Dataset CWRU2 under 120 training samples are demonstrated in Figs. 8 and 9, where the bearing fault states are distinguished by different colors.
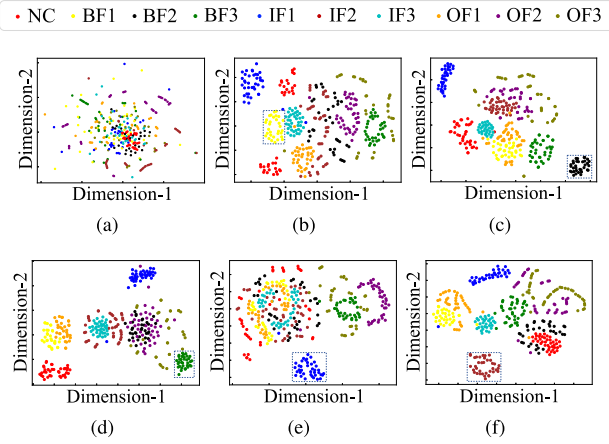
Fig. 8. Feature visualization of the PIBs. (a) Original data. (b)–(f) PIBs for fault types associated with labels of BF1, BF2, BF3, IF1, and IF2, respectively.
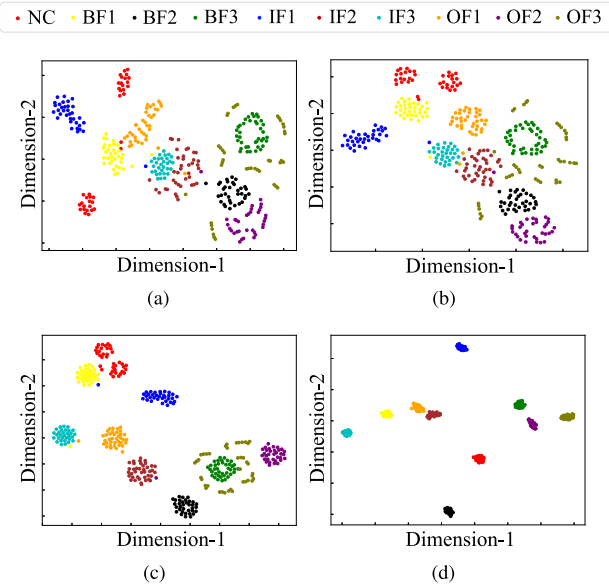

Fig. 9. Feature visualization of different layers in the MPINet. (a) Combine layer. (b) Dual path convolution module 1. (c) Dual path convolution module 2. (d) Max pooling layer.

Fig. 8 presents the original data and the features extracted by different trained PIBs. From the blue dashed boxes in Fig. 8(b)–(f), one can observe that each PIB enables a clear cluster formation for feature points of its target failure mode, in contrast with the unclear feature distribution of the original data points. These feature points can be initially distinguished from other fault types, indicating that incorporating physical knowledge specific to bearing faults equips the PIB with an efficient capability for feature extraction. In addition, it can be found that there is more than one cluster formed in the feature maps of each PIB. This is due to the fact that the physics convolution kernel of each PIB is generated according to the fault type of IF, BF, or OF, which would inevitably improve the ability of the PIB to recognize other faults at the same location but with different severity.

The output features of multiple layers in the classifier head of our MPINet, i.e., the Combine layer and two dual path convolution modules (referring to Fig. 2), are visualized in

Fig. 9. The process of clustering and separating data points with different fault types is demonstrated. As shown in Fig. 9(a), compared to the feature extracted by a single PIB, the fusion of multiscale features from multiple PIBs makes the separation phenomenon of different fault states more obvious. Data points of each failure mode are basically clustered and there is a certain distance between different classes. This indicates that the multiscale feature fusion mechanism has effectively promoted the information exchange between various PIBs and reduced the training cost of the MPINet. From Fig. 9(b) and (c), it is evident that the inclusion of the dual path convolution module leads to a reduction in intraclass distances among data points, while simultaneously increasing interclass distances. Finally, the max pooling layer [Fig. 9(d)] plays a crucial role in extracting the most critical features, thereby accelerating the training process.

IV. CONCLUSION

In this study, a novel MPINet was proposed for bearing fault diagnosis with small samples. The fundamental idea of our work is to leverage physical knowledge to enable the deep model could better learn fault features from small samples. To pursue this goal, two novel components, i.e., a feature extractor and a classifier head, were developed and used to construct our MPINet. To be specific, the feature extractor consisted of multiple PIBs for extracting multiscale fault features. Each PIB was used to incorporate the physical knowledge of particular failure modes into the coding process of the convolutional layer. A new training strategy was also developed to train each PIB by taking its target failure mode associated data as positive samples and all other samples as negative ones. In the classifier head, a new multiscale feature fusion structure was designed, which facilitated the information transfer between different PIBs and also enhanced the learning capability of the model. Extensive experimental results have shown that our proposed MPINet outperforms other methods by a large margin when the quantity of training samples is limited. The model also exhibits robust domain adaptation under different conditions and different bearing systems. It is beneficial in the timely warning and localization of failures in industrial equipment, as well as in assisting in prognosis.

It is worth noting that if the relevant physical mechanisms can be obtained to generate the physics kernel, our proposed MPINet method can also be extended to fault diagnosis tasks for other equipment (such as motors and pumps) or based on other monitoring signals (such as thermal images). In the future, our research endeavors could be extended to: 1) exploring and experimenting with different signals across different fields; and 2) establishing effective cross-domain diagnosis methods for cases where actual data is incomplete, such as when only unlabeled data or only normal data is available.

REFERENCES

[1] X. Chen, R. Yang, Y. Xue, M. Huang, R. Ferrero, and Z. Wang, "Deep transfer learning for bearing fault diagnosis: A systematic review since 2016," *IEEE Trans. Instrum. Meas.*, vol. 72, 2023, Art. no. 3508221.

[2] S. Luo, X. Huang, Y. Wang, R. Luo, and Q. Zhou, "Transfer learning based on improved stacked autoencoder for bearing fault diagnosis," *Knowl.-Based Syst.*, vol. 256, 2022, Art. no. 109846.

[3] D. Liu, L. Cui, and W. Cheng, "Flexible generalized demodulation for intelligent bearing fault diagnosis under nonstationary conditions," *IEEE Trans. Ind. Inf.*, vol. 19, no. 3, pp. 2717–2728, Mar. 2023.

[4] A. Glowacz, "Thermographic fault diagnosis of electrical faults of commutator and induction motors," *Eng. Appl. Artif. Intell.*, vol. 121, 2023, Art. no. 105962.

[5] M. Khanjani and M. Ezoji, "Electrical fault detection in three-phase induction motor using deep network-based features of thermograms," *Measurement*, vol. 173, 2021, Art. no. 108622.

[6] A. Glowacz, "Ventilation diagnosis of minigrinders using thermal images," *Expert Syst. Appl.*, vol. 237, 2024, Art. no. 121435.

[7] T. Chen and D. Yu, "A novel method for enhanced demodulation of bearing fault signals based on acoustic metamaterials," *IEEE Trans. Ind. Inf.*, vol. 18, no. 10, pp. 6857–6864, Oct. 2022.

[8] X. Ding, Y. Li, J. Xiao, Q. He, X. Yang, and Y. Shao, "Parametric doppler correction analysis for wayside acoustic bearing fault diagnosis," *Mech. Syst. Signal Process.*, vol. 166, 2022, Art. no. 108375.

[9] H. Guan, Y. Zhang, M. Xian, H.-D. Cheng, and X. Tang, "SMOTE-WENN: Solving class imbalance and small sample problems by oversampling and distance scaling," *Appl. Intell.*, vol. 51, pp. 1394–1409, 2021.

[10] D. Zhao et al., "Enhanced data-driven fault diagnosis for machines with small and unbalanced data based on variational auto-encoder," *Meas. Sci. Technol.*, vol. 31, no. 3, 2019, Art. no. 035004.

[11] J. Liu, F. Qu, X. Hong, and H. Zhang, "A small-sample wind turbine fault detection method with synthetic fault data using generative adversarial nets," *IEEE Trans. Ind. Inf.*, vol. 15, no. 7, pp. 3877–3888, Jul. 2019.

[12] Y. Dong, Y. Li, H. Zheng, R. Wang, and M. Xu, "A new dynamic model and transfer learning based intelligent fault diagnosis framework for rolling element bearings race faults: Solving the small sample problem," *ISA Trans.*, vol. 121, pp. 327–348, 2022.

[13] Y. Hu, R. Liu, X. Li, D. Chen, and Q. Hu, "Task-sequencing meta learning for intelligent few-shot fault diagnosis with limited data," *IEEE Trans. Ind. Inf.*, vol. 18, no. 6, pp. 3894–3904, Jun. 2022.

[14] H. Liang, J. Cao, and X. Zhao, "Multibranch and multiscale dynamic convolutional network for small sample fault diagnosis of rotating machinery," *IEEE Sens. J.*, vol. 23, no. 8, pp. 8973–8988, Apr. 2023.

[15] S. Plakias and Y. S. Boutalis, "Fault detection and identification of rolling element bearings with Attentive Dense CNN," *Neurocomputing*, vol. 405, pp. 208–217, 2020.

[16] S. Shen et al., "A physics-informed deep learning approach for bearing fault detection," *Eng. Appl. Artif. Intell.*, vol. 103, 2021, Art. no. 104295.

[17] G. Maruthi and V. Hegde, "Application of MEMS accelerometer for detection and diagnosis of multiple faults in the roller element bearings of three phase induction motor," *IEEE Sens. J.*, vol. 16, no. 1, pp. 145–152, Jan. 2016.

[18] C. Szegedy et al., "Going deeper with convolutions," in *Proc. IEEE Conf. Comput. Vis. Pattern Recognit.*, 2015, pp. 1–9.

[19] M. Sadoughi and C. Hu, "Physics-based convolutional neural network for fault diagnosis of rolling element bearings," *IEEE Sens. J.*, vol. 19, no. 11, pp. 4181–4192, Jun. 2019.

[20] P. McFadden and J. Smith, "Model for the vibration produced by a single point defect in a rolling element bearing," *J. Sound Vib.*, vol. 96, no. 1, pp. 69–82, 1984.

[21] Y. Wang, G. Xu, Q. Zhang, D. Liu, and K. Jiang, "Rotating speed isolation and its application to rolling element bearing fault diagnosis under large speed variation conditions," *J. Sound Vib.*, vol. 348, pp. 381–396, 2015.

[22] W. A. Smith and R. B. Randall, "Rolling element bearing diagnostics using the case western reserve university data: A benchmark study," *Mech. Syst. Signal Process.*, vol. 64, pp. 100–131, 2015.

[23] MFPT, "MFPT dataset," Accessed: Aug. 14, 2023 [Online]. Available: https://www.mfpt.org/fault-data-sets/

[24] M. Wang et al., "Roller bearing fault diagnosis based on integrated fault feature and SVM," *J. Vib. Eng. Technol.*, vol. 10, pp. 853–862, 2021.

[25] S. Xie, Y. Li, H. Tan, R. Liu, and F. Zhang, "Multi-scale and multi-layer perceptron hybrid method for bearings fault diagnosis," *Int. J. Mech. Sci.*, vol. 235, 2022, Art. no. 107708.

[26] K. He, X. Zhang, S. Ren, and J. Sun, "Identity mappings in deep residual networks," in *Proc. Eur. Conf. Comput. Vis.*, 2016, pp. 630–645.

[27] W. Zhang, C. Li, G. Peng, Y. Chen, and Z. Zhang, "A deep convolutional neural network with new training methods for bearing fault diagnosis under noisy environment and different working load," *Mech. Syst. Signal Process.*, vol. 100, pp. 439–453, 2018.

[28] C. Liu and K. Gryllias, "Simulation-driven domain adaptation for rolling element bearing fault diagnosis," *IEEE Trans. Ind. Inf.*, vol. 18, no. 9, pp. 5760–5770, Sep. 2022.

Chao Gao received the B.S. and M.S. degrees in naval architecture and ocean engineering from Harbin Engineering University, Harbin, China, in 2016 and 2019, respectively. She is currently working toward the Ph.D. degree in ocean engineering with the School of Ocean and Civil Engineering, Shanghai Jiao Tong University, Shanghai, China.

Her research interests include fault diagnosis, reliability analysis, and prognostics and health management.

Zikai Wang (Graduate Student Member, IEEE) received the M.S. degree in naval architecture and ocean engineering from Harbin Engineering University, Harbin, China, in 2019. He is currently working toward the Ph.D. degree in software engineering with the School of Computer Science and Technology, Soochow University, Suzhou, China.

His research interests include low-level feature detection, signal processing, and 3-D reconstruction.

Yongjin Guo received the Ph.D. degree in naval architecture and ocean engineering from Shanghai Jiao Tong University, Shanghai, China, in 2020.

From 2020 to 2022, he was a Postdoctoral Researcher with the Department of Engineering Mechanics, Shanghai Jiao Tong University. Since 2023, he has been with the Faculty of the School of Ocean and Civil Engineering, Shanghai Jiao Tong University. His research interests include reliability design, reliability testing, and health management of intelligent ships.

Hongdong Wang received the B.S., M.S., and Ph.D. degrees in naval architecture and ocean engineering from Shanghai Jiao Tong University, Shanghai, China, in 2011, 2014, and 2016, respectively.

He is currently a Professor with the School of Ocean and Civil Engineering, Shanghai Jiao Tong University. He has authored or coauthored more than 60 papers, obtained over 20 patents, edited one English academic monograph, and participated in the enactment of one national standard. His research interests include intelligent control and ship maneuvering models.

Dr. Wang has been awarded as Young Chang Jiang Scholar by the Chinese Ministry of Education. He now serves as the Secretary General of the Youth Committee affiliated to the Chinese Society of Naval Architects and Marine Engineers.

Hong Yi received the Ph.D. degree in naval architecture and ocean engineering from Shanghai Jiao Tong University, Shanghai, China, in 2002.

He is currently a Professor with the School of Ocean and Civil Engineering, Shanghai Jiao Tong University. His current research interests include system reliability analysis, virtual reality, and human factors engineering.